www.sciencemag.org/content/358/6362/502/suppl/DC1

Supplementary Materials for

Toughening elastomers using mussel-inspired iron-catechol complexes

Emmanouela Filippidi, Thomas R. Cristiani, Claus D. Eisenbach, J. Herbert Waite, Jacob N. Israelachvili, B. Kollbe Ahn, Megan T. Valentine*

*Corresponding author. Email: valentine@engineering.ucsb.edu

Published 27 October 2017, *Science* **358**, 502 (2017)
DOI: 10.1126/science.aao0350

This PDF file includes:

Supplementary Materials:

Materials and Methods

Materials

The polymer poly(ethylene glycol) diglycidyl ether (PEG-diepoxide), cross-linker 1,4-diaminobutane, benzyl control group (2,3-epoxypropyl)benzene, hydrochloric acid, iron(III) nitrate nonahydrate, tetrahydrofuran, bicine, sodium hydroxide, trace metal grade sulfuric acid, and trace metal grade hydrogen peroxide were all purchased from Sigma Aldrich. The protected catechol species, 2-[[3,4-bis[(triethylsilyl)oxy]phenyl]methyl]oxirane was kindly donated from Osaka Organic Chemical Industry.

Methods

Network synthesis and treatment

Polymer networks were synthesized by mixing the monomers per the compositions in Table 1 and degassing for 3 min at mtorr pressures. The monomer mixtures were then cured between hydrophobized glass slides at 60 °C and 450 torr for 12-15 hours. The 0.5 mm polymer films were then cut into D638 ASTM standard dog bone specimens using a steel punch. Specimens were then deprotected by submerging in 350 ml of degassed HCl at pH 2.5 for 24 hours. The solution was exchanged for fresh HCl every 2 hours for the first 6 hours of deprotection. After deprotection, the swollen specimens were immediately transferred to a 200-ml solution of 0.2 M bicine and 0.05 M $Fe(NO_3)_3 \cdot 9H_2O$, titrated to pH 7.5 with NaOH, and kept submerged for 24 hours. All samples – protected, deprotected, and iron-treated – were dried at 30 °C and 125 torr in a vacuum oven for 24 hours before any measurements were performed. All dry measurements were taken immediately after removing the samples from vacuum. Samples for tensile measurements under wet conditions were never dried. Instead, after iron incorporation, they were immersed in degassed deionized water for 24 hours. Samples for tensile measurements taking place before and after exposure to ambient conditions were dried in a vacuum oven at 30 °C and 200 torr for over 24 hours and then either exposed for 1 hour to 21.5 °C and 41% relative humidity, or to 22 - 24 °C and 40 - 35% relative humidity for 7.5 hours. For comparison, samples were dried at a lower pressure at 100 torr, and then immediately pulled to fracture. To study the effects of induced oxidation, samples were placed into non-degassed deionized water immediately after iron incorporation, stored for either two or five days, then dried at 30 °C and 200 torr for 24 hours, and subsequently subjected to tensile testing.

Fourier-transform infrared (FTIR) spectroscopy

The network-curing epoxy-amine reaction was monitored in time with FTIR spectroscopy (Magna-IR 850, Series II by Nicolet). The separate reactants and the mixed solution were measured in between ZnSe windows and the entire assembly was placed at 60 °C. The IR spectra (7250-1000 cm^{-1}) were monitored at regular time intervals for the curing reactions of Networks 1, 2, and 4 (Table S1). The disappearance of the normalized, background-subtracted areas of the bands centered at 4940 cm^{-1} (primary amine) and 4520 cm^{-1} (epoxide) were monitored with time. The extent of reaction, X_t^i, of a given functional group, *i*, at total curing time, *t*, was

calculated by dividing the difference between the area, A_t^i, of the corresponding IR band at $t = 0$ and the area at t by the area of the band at $t = 0$ (*27*, *28*):

$$X_t^i = \frac{A_{t=0}^i - A_t^i}{A_{t=0}^i}$$

Rheology

Rheometry was performed using a ARES-G2 by TA Instruments with a cone-and-plate geometry (2°, 40 mm diameter) at the curing temperature of 60 °C, 0.1% strain amplitude, and 10 rad/s angular frequency. The time evolution of the loss (G'') and storage (G') moduli was measured for the protected catechol network starting from the mixture of the monomers.

Differential scanning calorimetry (DSC)

DSC was performed (TA Instruments Q2000) in the range of −100 °C to 50 °C with a heating and cooling rate of 5 °C/min. Final data were collected for two full cycles which were identical. The results of the second cycle are shown (Fig. S4). Preliminary data were taken for three full cycles at 10 °C/min, which again were identical. The inflection points of the DSC traces were used for the determination of the glass transition temperatures, T_g.

X-ray photoelectron spectroscopy (XPS)

XPS was performed on a Kratos Axis Ultra DLD XPS system using a monochromated Al source (1486 eV). Survey scans were run at a pass energy of 160 eV, and high-resolution scans were run at 20 and 40 eV. A low-energy electron flood was used to neutralize charge, and the energy scale was calibrated by fitting the high-resolution aliphatic carbon 1s peak to 285.0 eV.

Resonance Raman spectroscopy

The interior surfaces of cross-sections were used to collect Raman spectra (Horiba, LabRAM Aramis spectrometer with confocal microscope) with a 785-nm laser line with the spectrometer pinhole and slit each set to 400 μm. Each spectrum is the average of 100 exposures of 500 ms each.

Inductively-coupled plasma atomic emission spectrometry (ICP-AES)

ICP-AES (Thermo iCAP 6300) was performed on samples previously digested in piranha (5:1 sulfuric acid:hydrogen peroxide, trace metal grade) and diluted to a parts per million concentration with Milli-Q water (resistivity of 18 MΩ).

Scanning electron microscopy (SEM) and energy dispersive X-ray spectroscopy (EDX)

For SEM, 20 μm thick cross-sections, sectioned with the Leica CM1850 cryostat at −28.3 °C, were sputter coated with gold/palladium 60/40, 99.99% (Hummer 6.2, Anatech, USA) for 90 seconds and imaged in backscattered mode with a scanning electron microscope (FEI XL30 Sirion FEG with EDX) using accelerating voltages of 5 kV. EDX was performed at 15 kV, more than double the K-edge absorption energy of iron.

Transmission electron microscopy (TEM, STEM-HAADF)

For TEM, 70 nm thin cross-sections were sliced with the Leica EM FC7 cryo-ultramicrotome using a diamond knife at −80 °C, significantly below the glass transition temperature of all

samples. High resolution TEM (HRTEM, FEI Titan at 300 kV, $\lambda = 1.96$ pm) was performed to check for the presence of small precipitates with crystalline order. In addition, scanning TEM (STEM) was performed in a high angle annular dark-field STEM (HAADF-STEM) configuration to check for any clustering of iron atoms. The higher atomic number of iron, 26, compared to carbon, oxygen, and hydrogen (6, 8, and 1 respectively), ensures that any clustering of iron would lead to brighter regions in a STEM- HAADF image due to the greater incoherent scattering of electrons by heavy nuclei.

Small- and wide-angle X-ray scattering (SAXS and WAXS)

SAXS and WAXS measurements were conducted using a custom constructed SAXS instrument in the X-ray diffraction facility in the Materials Research Laboratory (MRL). The instrument uses a 50-μm microfocus, Cu target X-ray source (wavelength, $\lambda = 1.54$ Å) with parallel-beam multilayer optics and monochromator (Genix from XENOCS SA, France), high efficiency scatterless hybrid slits collimator developed in house (*29*), and Pilatus100k and Eiger 1M solid state detectors (Dectris, Switzerland). A built-in temperature stage that houses the sample was used for the 40 °C and 60 °C SAXS measurements (Fig. S6).

Tensile testing

Uniaxial tensile testing was performed on 0.5 mm thick dog bone-shaped specimens (shown in Fig. 1C-D) according to the ASTM D638 standard, on a custom-built setup on a vertical TwinRail positioning table (Lintech, CA) with a 10-lb load cell (3108-10, Eaton Corp., MI) fitted with a laser extensometer (LE-01, Electronic Instrument Research, PA). Cyclic-loading experiments were held at zero force between cycles by reducing the applied strain as specimens contracted.

Stress relaxation

Samples were first loaded uniaxially at a strain rate of $\dot{\varepsilon} = 10\ \text{min}^{-1}$ to a strain of $\varepsilon = 0.6$. Load and strain are measured with time at constant grip displacement.

Dynamic mechanical analysis

DMA was performed at the Cornell Center for Materials Research. Experiments were conducted under tension in nitrogen atmosphere (Q800, TA Instruments) on iron-treated rectangular samples of dimension 7.5749 mm × 4.9100 mm × 0.5 mm. A tensile preload force of 0.01 N was applied and small oscillations of amplitude 0.05% strain applied at 1 Hz frequency. A temperature sweep from −120 °C to 70 °C was performed with a rate of 2 °C/min.

Supplementary text

Rate-dependent uniaxial tensile stress-strain curves, Figure 3B

We calculate the slopes $S_{0.1}$, S_1, S_{10} corresponding to the segment $\sigma(\varepsilon > 1)$ for strain rates 0.1, 1, and 10 respectively. The slopes of these linear segments increase with strain rate from $S_{0.1} = 7.1 \pm 0.6$ MPa to $S_1 = 11.5 \pm 0.6$ MPa and $S_{10} = 14.2 \pm 0.4$ MPa. As this slope occurs post-yielding, significant rearrangements have occurred compared to the original unstretched system. Increasing the tensile strain rate does not allow time for the coordination bonds to explore configurations and increases the resistance to dissociation, therefore increasing S. Furthermore,

as the duration of the experimental run (the time to reach fracture) is very short, 0.4 min for the 10 min^{-1} strain rate versus 41 min for the 0.1 min^{-1} rate, there is not sufficient time to form stress-free coordination complexes. At slower strain rates, stress-free complexes can form, however the decreased slope shows that the increased number of reformed bonds cannot increase *S* sufficiently to compete with the softening due to ample time given for bonds and chains to explore new configurations and dissociate.

Predicting the *q*-shifts in SAXS ionomer peaks

The atomistic simulations of Bolintineanu et al. (*28*) predict for linear ionomers that changing the spacing between ionic side chains correspondingly changes the SAXS correlation distance between the 'ionomer peaks.' The ionomer peak measures the average distance, *r*, between ionomer clusters. This distance is related to the number of chain segments, *n*, between clusters by:

$$\langle r^2 \rangle = C_\infty n l^2$$

where *l* is the length of a single chain segment and C_∞ is the characteristic ratio for the ionomer backbone. For the same backbone of sufficient length, C_∞ and *l* will be invariant, yielding the expression:

$$\frac{\langle r_1^2 \rangle}{n_1} = \frac{\langle r_2^2 \rangle}{n_2}$$

Where subscripts denote polymers with different chain lengths between ionomer side groups. Thus, for two networks with Gaussian chains, the relationship between the ionomer peaks will be:

$$\langle r_2 \rangle = \langle r_1 \rangle \sqrt{\frac{n_2}{n_1}}$$

In the present work, the iron-treated 50% BENZ network has twice the average spacing between catechol groups as compared to the iron-treated 100% CAT network; therefore, $n_{50\%} = 2n_{100\%}$ and $r_{50\%} = r_{100\%}\sqrt{2}$. The measured values for $r_{50\%}$ and $r_{100\%}$ from SAXS (Fig. 2D) are 12.2 ± 0.8 and 8.57 ± 0.02 nm, respectively, and $\frac{12.2 \pm 0.08 \text{ nm}}{8.57 \pm 0.02 \text{ nm}} = 1.42 \pm 0.09 \approx \sqrt{2}$.

Table S1 - Polymer Network Compositions. Monomer composition of reaction mixtures for each cured network. Tetrahydrofuran (4 wt% of neat monomers) was added as a compatibilizer to each reaction mixture.

Network 1 – PEG-DE:CAT:DAB = 1.00:1.54:0.88 – "Protected, 100% CAT"				
	PEG-DE	**DAB**	**CAT**	
Mass Percent	42.2	6.6	51.2	
Mole Percent	29.2	25.8	45.0	
Mole Percent Constitutive Units	77.8	8.1	14.1	
Network 2 – PEG-DE:BENZ:DAB = 1.00:1.54:0.88 – "100% BENZ"				
	PEG-DE	**DAB**	**(2,3-epoxypropyl)benzene**	
Mass Percent	63.8	9.9	26.3	
Mole Percent	29.2	25.8	45.0	
Mole Percent Constitutive Units	77.8	8.1	14.1	
Network 3 – PEG-DE:CAT:BENZ:DAB = 1.00:0.77:0.77:0.88 – "Protected, 50% BENZ"				
	PEG-DE	**DAB**	**(2,3-epoxypropyl)benzene**	**CAT**
Mass Percent	50.8	7.9	10.5	30.8
Mole Percent	29.2	25.8	22.5	22.5
Mole Percent Constitutive Units	77.8	8.1	7.05	7.05
Network 4 – PEG-DE:DAB = 1.00:0.50 – "No aromatic species"				
	PEG-DE	**DAB**		
Mass Percent	91.9	8.1		
Mole Percent	66.7	33.3		
Mole Percent Constitutive Units	94.5	5.5		

The monomer stoichiometries for Networks 1-3 were chosen to maximize the total composition of their respective monofunctional species while maintaining a fully-crosslinked network at very low cross-link density. The kinetic model presented by Cheng (*19*) describes exactly the type of epoxy-system we have synthesized (a bisepoxide/diamine system with a monoepoxide diluent). This model predicts a very slightly cross-linked, gelled network for a ratio, *s*, of [epoxy functional groups originating from monoepoxides] to [epoxy functional groups originating from bisepoxides], between 0.6 and 0.8. For the networks studied, $s = 0.77$ was chosen to maximize monoepoxide content while maintaining a true network and not creating a merely hyper-branched system.

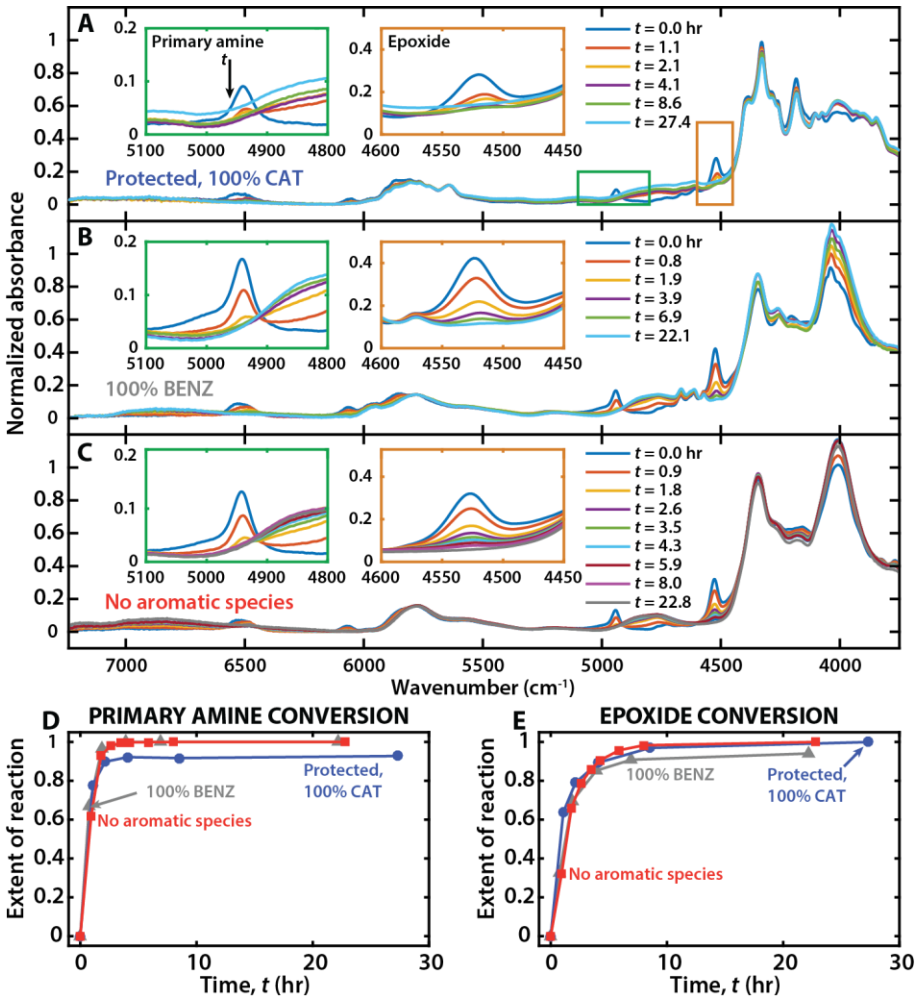

Fig. S1. Fourier transform infrared spectroscopy of benzyl- and catechol-containing networks. (A-C) FTIR spectra taken at different times during the curing of the (A) protected, 100% catechol network (Network 1), (B) the 100% benzyl network (Network 2), and (C) a network containing no aromatic species (Network 4). The spectra were normalized to an invariant band centered at approximately 1960 cm^{-1} (not shown), which is a skeletal band corresponding to the PEG backbone. A combination band of NH stretching and bending from the primary amines is centered at 4940 cm^{-1} and has been enlarged in the green insets (left). The combination band of the second overtone of the epoxide ring stretching and the fundamental CH stretching is centered at 4520 cm^{-1} and has been enlarged in the orange insets (right). The bands centered around 6500 cm^{-1} are due to both primary and secondary amines and cannot easily be used quantitatively. However, with increasing conversion, these bands exhibit a shift towards lower wavenumbers before disappearing, an indication of conversion of both primary amine to secondary amine and secondary amine to tertiary amine. **(D, E)** Conversion of (D) primary amine groups and (E) epoxide groups vs. curing time for all three networks (Network 1, red squares; Network 2, gray triangles; Network 4, blue circles).

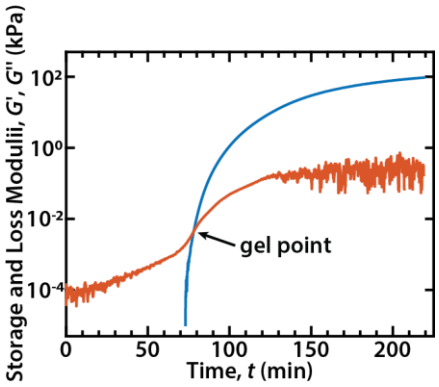

Fig. S2. Bulk, oscillatory rheology demonstrates gelation. Measurement of storage (G') and loss (G'') moduli during curing at 60 °C, starting from the liquid monomer mixture of Network 1. The cross-over of G' and G'' is indicative of the gelation and corresponds to an epoxy conversion of 67% and primary amine conversion of 80% (Fig. S1 D-E) as monitored by IR spectroscopy. This measurement suggests a large difference in the reactivity of the PEG-DE epoxide groups and the CAT epoxide groups (*19*). According to Cheng *et al*., for a monoepoxide:bisepoxide ratio of $s = 0.77$, a gel-point epoxide conversion of 67% would correspond to a ratio of activities of monoepoxide:bisepoxide, $\lambda \approx 0.2$. This value for λ is reasonable, given the steric bulk, and therefore reduced mobility, of the CAT moiety. The storage modulus after complete curing ($t >$ 220 min), $G'_{max} \approx 100$ kPa, is within the appropriate order of magnitude as compared to the tensile modulus of the protected Network 1, $E_{prot} = 240$ kPa, given the expression $E = (2G')(1+\nu)$.

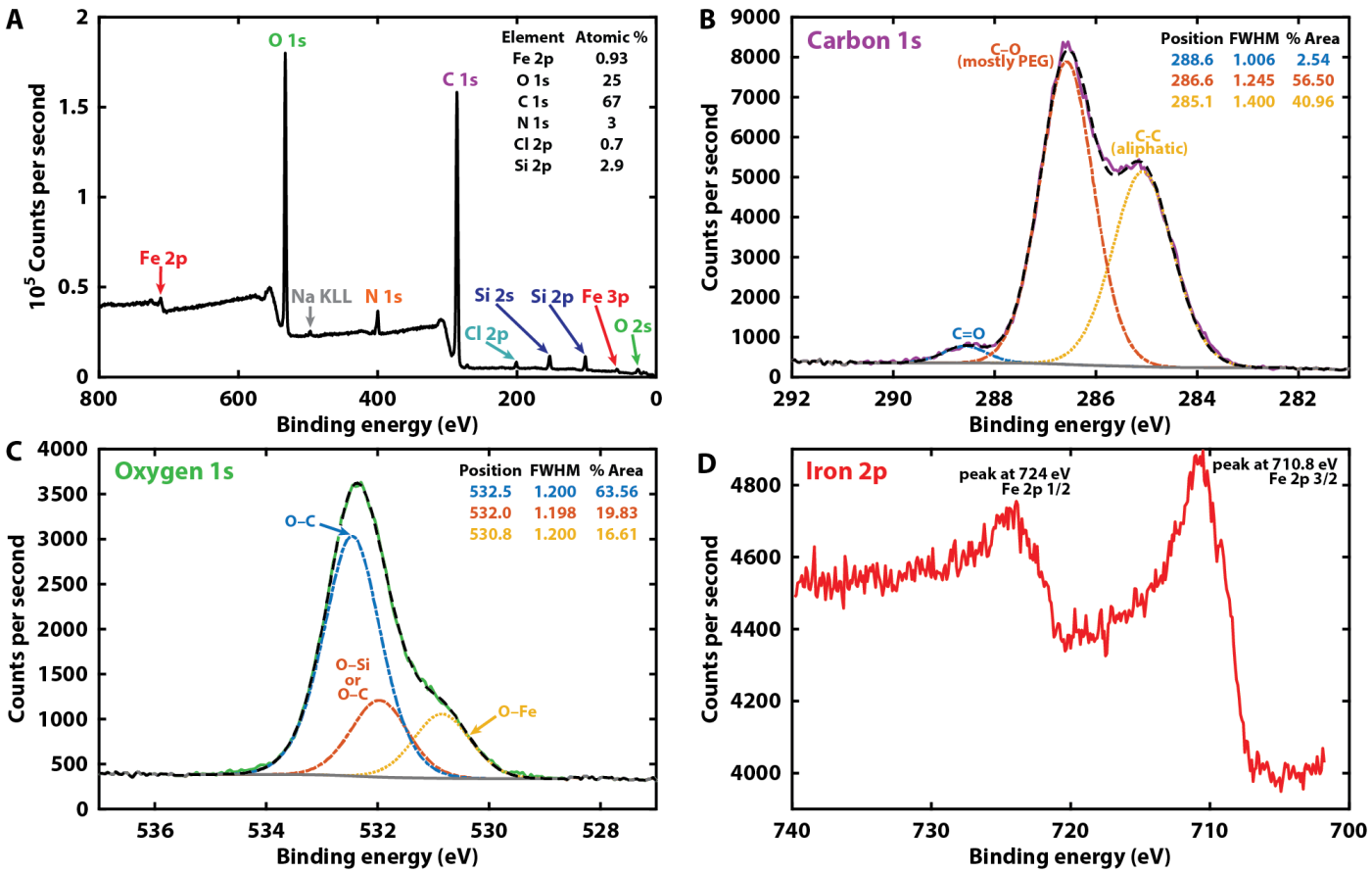

Fig. S3. X-ray photoelectron spectroscopy (XPS) scans. (A) Survey scan **(B)** Carbon shifts. The largest peak is attributed to the PEG C-O binding. **(C)** Oxygen shifts. Corresponding to the largest carbon peak, we attribute the largest oxygen peak to the PEG O-C binding. The lower binding energy shift is attributed to O-Fe binding and in particular C-O-Fe binding. Fe-O-Fe binding according to the chemistry proposed in (*30*) is not supported by the O shifts as it should occur at lower binding energies than the O-Fe peak. The area of the C-O-Fe binding curve corresponds to 16.61% of the total atomic percentage of oxygen, so 4.46% of total atomic mass. From the survey scan, the iron is 0.93% of total atomic mass, therefore we can estimate 4.46 non-water oxygen atoms per iron atom, supporting mixed bis- and tris- iron-catechol coordination. **(D)** Iron shifts. The low content of iron leads to a low signal-to-noise ratio. However, comparison of the peak in our data at 710.8 eV with tabulated values which give the Fe2p3/2 for Fe_2O_3 at 710.8 eV versus 709.6 eV for FeO, supports the presence of Fe(III) versus Fe(II).

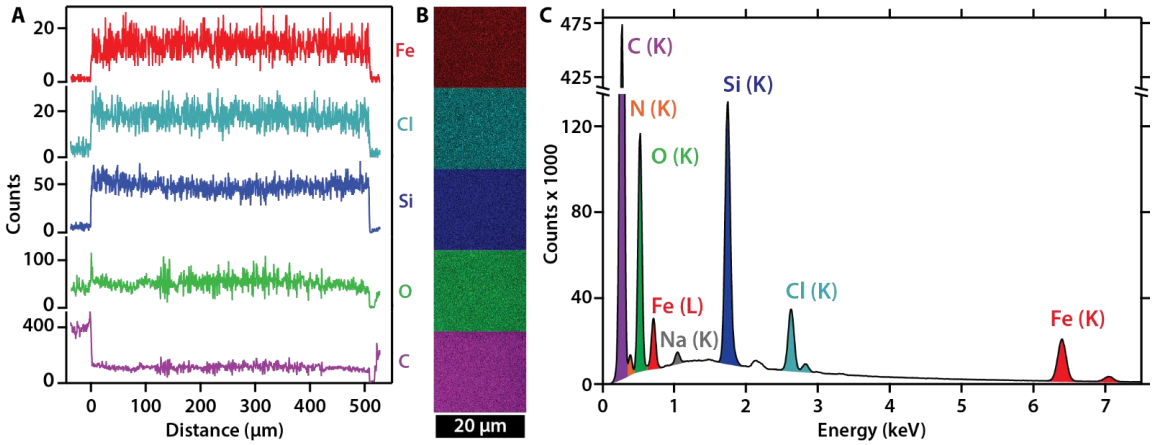

Fig. S4. Energy dispersive X-ray (EDX) scans of a sample cross-section. (A) Line scans across the sample thickness of all elements of interest: Fe, Cl, Si, O and C. The sample used and scan line measured are shown in Fig. 2B. All species show uniform distribution along the measured line-scan. **(B)** Area scans of the nearby regions confirm uniformity. **(C)** Spectrum corresponding to the area scans collected in (B) showing the signal and the Bremsstrahlung radiation background.

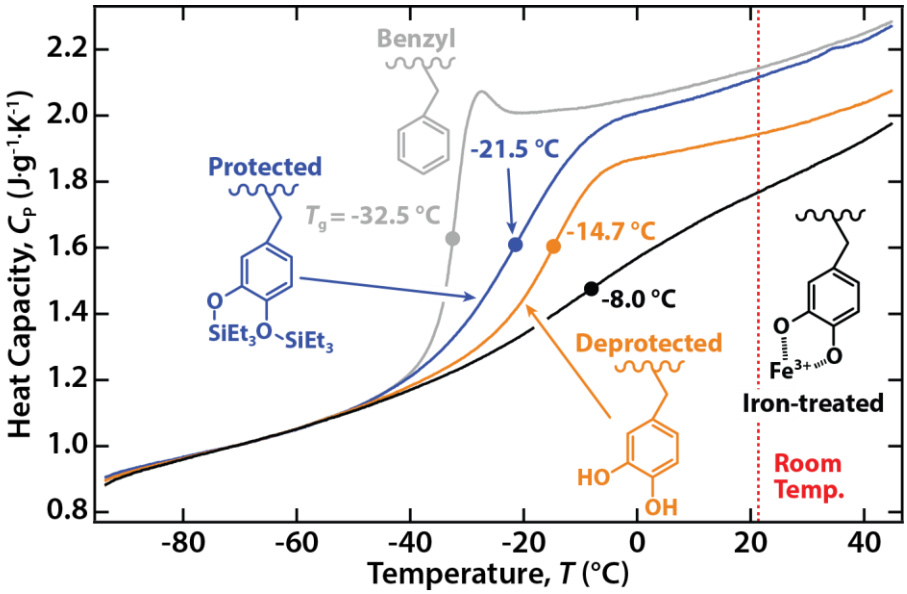

Fig. S5. Differential scanning calorimetry (DSC) of benzyl, protected, deprotected and iron-treated samples. Specific heat capacity as a function of temperature. The iron-treated curve is arbitrarily shifted in C_p to illustrate both the broadening and the ΔC_p associated with the glass transition. All samples have T_g values (filled circles) below room temperature.

The benzyl-containing sample exhibits a typical glass transition curve with T_g = −32.5 ± 0.4 °C. The protected catechol-containing sample with the bulky protecting groups exhibits reduced rotational freedom, in accordance with the crankshaft model, and a broadening of the glass transition with T_g −21.5 ± 0.5 °C. Even though the transition starts at the same temperature, it ends at a higher temperature depicting the additional energy needed to overcome the lack of rotational freedom. However, the same ΔC_p is reached. The deprotected catechol sample shows a delay in the onset of the glass transition and a reduced ΔC_p, leading to an even higher T_g of −14.7 ± 0.5 °C. The deprotected catechols' ability to hydrogen bond fortuitously balances the lack of a bulky deprotecting group which would have driven T_g to a lower value. The net effect is a delay in the onset of the transition. The iron-treated sample exhibits a pronounced broadening with a T_g of −8.0 ± 0.6 °C. The presence of covalent and coordination bonds that act as cross-links, the polydispersity of the distances between them, and the multiple relaxation processes with varying timescales introduced due to the two types of bonding as well as the spatial segregation of catechols lead to the broadening of the transition. Dynamic mechanical analysis (DMA) data shown in Fig. S6 provide a more detailed measurement of the broad glass transition measured by DSC.

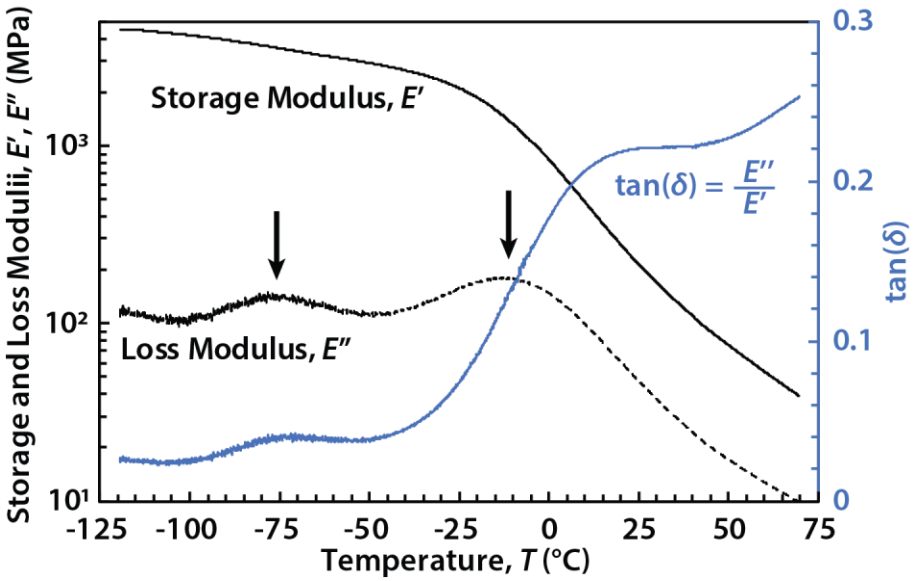

Fig. S6. Storage (*E′*) and loss (*E″*) moduli, and tan(δ) of the iron-treated network measured by dynamic mechanical analysis (DMA). The storage modulus, *E′* (black line) exhibits a broad decay with increasing temperature, never reaching a rubbery state (where *E′* would be linearly increasing with temperature). The long transition also reflects the broad glass transition observed in DSC. The drop of *E′* coincides with the peak of *E″* at −13 °C, which is in good agreement with the glass transition T_g measured by DSC, considering the difference in heating rate. The two peaks of *E″* (indicated by black arrows) suggest a phase-separated system at very low temperatures, possibly correlated with the ionomer-like domains. At temperatures above 50 °C, which in DSC correspond to a region beyond the glass transition, tan(δ) (blue line) does not decrease. This suggests that the broad glass transition arises from a combination of multiple relaxations that are intrinsic to the designed system that contains both covalent bonds and iron-catechol dynamic coordinate bonds.

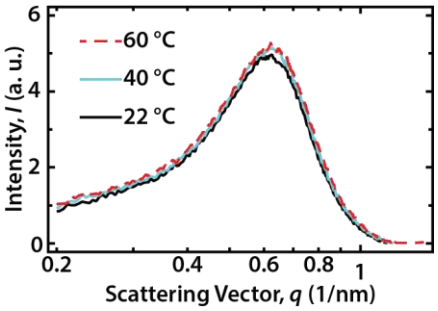

Fig. S7. Small-angle X-ray scattering (SAXS) of iron-treated 100% CAT network as a function of temperature. The so-called 'ionomer peak' does not change with temperature, indicating that the structure, spacing, and shape of the electron dense regions are static despite the energy input.

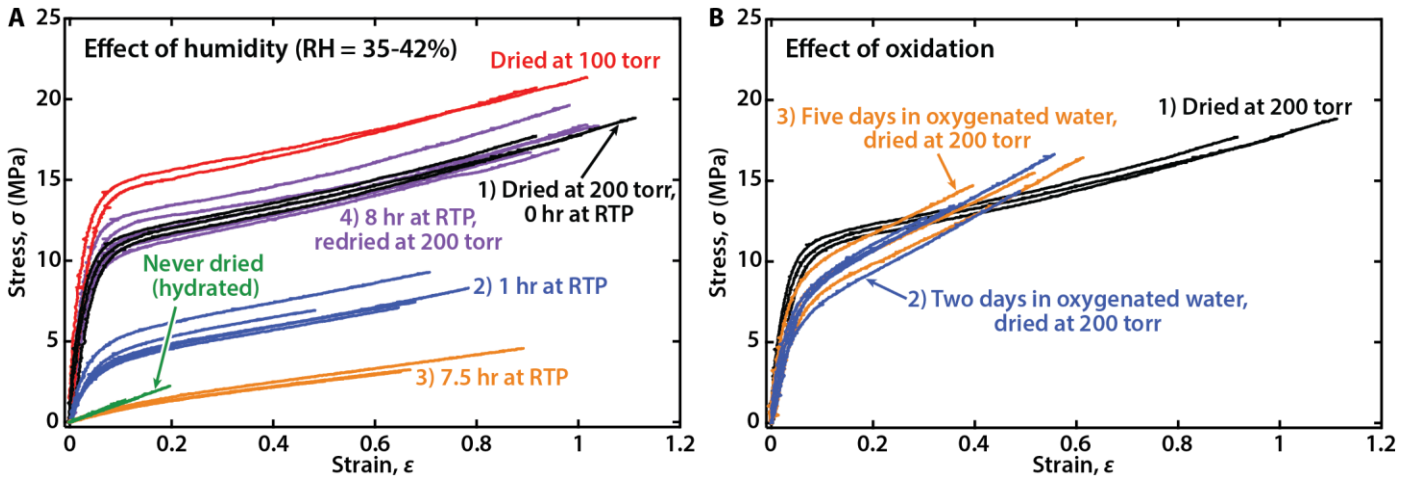

Fig. S8. Effect of relative humidity and oxidative conditions on the tensile properties of the iron-treated material pulled at a strain rate of 1 min^{-1}. (**A**) Wet iron-treated specimens (green) exhibit a linear stress-strain relation (E_{wet} = 5.7 ± 0.4 MPa, N = 4) and a reduction in maximum strain to fracture (~20%) as one would expect for a hydrogel, compared to specimens dried at 200 torr (black, E = 141 ± 35 MPa, N = 3). The hydrophilic nature of PEG implies fully hydrated chains, constricted only by the covalent and hydrated iron-catechol complexes. Exposure to ambient conditions, T = 21.5 °C and relative humidity, RH = 41%, for 1 hr causes a significant decrease in mechanical performance (blue). The Young's modulus drops to 39 ± 7 MPa (N = 5) and the maximum strain to fracture is reduced. The effect can be attributed to three factors: (i) water slightly shifts the iron(III)-catechol equilibrium away from complex formation, effectively reducing the number of complexes by an exceedingly small amount; (ii) water acts a plasticizer and reduces inter-chain interactions, and, most importantly, (iii) water causes increased charge screening of the coordination complexes with the ionomeric domains. The effect is exacerbated after longer exposure (7.5 hr) to ambient conditions (orange, E = 5.1 ± 1.2 MPa, N = 4). However, re-drying the exposed samples at the same pressure (purple) largely removes all humidity effects, recovering both the modulus (E = 118 ± 17 MPa, N = 5) and the maximum strain at fracture to their original values, within error. This recovery strongly suggests that humidity only imparts physical changes in the network (not chemical changes, such as catechol oxidation). Drying the network at lower pressure (100 torr, red curves) with no exposure to ambient conditions further increases the network's modulus to E = 256 ± 63 MPa, N = 2, by removing even more water. (**B**) The effect of exposing the iron-treated specimens to non-degassed water accelerates the oxidative cross-linking of catechol. For the oxidized samples, there is a small decrease in the initial modulus, which is dominated by the coordination bonds, from E = 141 ± 35 MPa in the non-oxidized material, to E = 87 ± 22 MPa, N = 3 after two-day exposure in water (blue) and E = 106 ± 28 MPa, N = 3 five-day exposure (orange). Assuming catechol oxidative cross-linking only increases the overall cross-link density, one would expect oxidation to further increase the elastic modulus. However, this is not what we observe. Other explanations are necessary, such as iron oxidation, which reduces the amount of iron available for complex formation, or the disruption of the complexes due to the oxidative coupling of catechol. The combination of these effects may cause a net reduction in elastic modulus with a small amount of oxidation caused by a short exposure to ambient conditions. However, the increase in modulus after five days of oxidation compared to two days may reflect that oxidative cross-linking has begun to dominate. The major effect of oxidative cross-linking is observed

post-yield, when the coordination bonds start dissociating, with a markedly stiffer behavior dominated by a more cross-linked covalent network due to oxidative cross-linking. The higher density of covalent cross-links also leads to a lower maximum strain to fracture.

References and Notes

1. N. Domun, H. Hadavinia, T. Zhang, T. Sainsbury, G. H. Liaghat, S. Vahid, Improving the fracture toughness and the strength of epoxy using nanomaterials—a review of the current status. *Nanoscale* **7**, 10294–10329 (2015). doi:10.1039/C5NR01354B Medline

2. E. Ducrot, Y. Chen, M. Bulters, R. P. Sijbesma, C. Creton, Toughening elastomers with sacrificial bonds and watching them break. *Science* **344**, 186–189 (2014). doi:10.1126/science.1248494 Medline

3. E. Ducrot, C. Creton, Characterizing large strain elasticity of brittle elastomeric networks by embedding them in a soft extensible matrix. *Adv. Funct. Mater.* **26**, 2482–2492 (2016). doi:10.1002/adfm.201504536

4. K. Ohmori, I. Abu Bin, T. Seki, C. Liu, K. Mayumi, K. Ito, Y. Takeoka, Molecular weight dependency of polyrotaxane-cross-linked polymer gel extensibility. *Chem. Commun. (Camb.)* **52**, 13757–13759 (2016). doi:10.1039/C6CC07641F Medline

5. N. Holten-Andersen, M. J. Harrington, H. Birkedal, B. P. Lee, P. B. Messersmith, K. Y. C. Lee, J. H. Waite, pH-induced metal-ligand cross-links inspired by mussel yield self-healing polymer networks with near-covalent elastic moduli. *Proc. Natl. Acad. Sci. U.S.A.* **108**, 2651–2655 (2011). doi:10.1073/pnas.1015862108 Medline

6. D. Mozhdehi, S. Ayala, O. R. Cromwell, Z. Guan, Self-healing multiphase polymers via dynamic metal-ligand interactions. *J. Am. Chem. Soc.* **136**, 16128–16131 (2014). doi:10.1021/ja5097094 Medline

7. D. D. Lane, S. Kaur, G. M. Weerasakare, R. J. Stewart, Toughened hydrogels inspired by aquatic caddisworm silk. *Soft Matter* **11**, 6981–6990 (2015). doi:10.1039/C5SM01297J Medline

8. J. A. Neal, D. Mozhdehi, Z. Guan, Enhancing mechanical performance of a covalent self-healing material by sacrificial noncovalent bonds. *J. Am. Chem. Soc.* **137**, 4846–4850 (2015). doi:10.1021/jacs.5b01601 Medline

9. M. Burnworth, L. Tang, J. R. Kumpfer, A. J. Duncan, F. L. Beyer, G. L. Fiore, S. J. Rowan, C. Weder, Optically healable supramolecular polymers. *Nature* **472**, 334–337 (2011). doi:10.1038/nature09963 Medline

10. T. L. Sun, T. Kurokawa, S. Kuroda, A. B. Ihsan, T. Akasaki, K. Sato, M. A. Haque, T. Nakajima, J. P. Gong, Physical hydrogels composed of polyampholytes demonstrate high toughness and viscoelasticity. *Nat. Mater.* **12**, 932–937 (2013). doi:10.1038/nmat3713 Medline

11. J.-Y. Sun, X. Zhao, W. R. K. Illeperuma, O. Chaudhuri, K. H. Oh, D. J. Mooney, J. J. Vlassak, Z. Suo, Highly stretchable and tough hydrogels. *Nature* **489**, 133–136 (2012). doi:10.1038/nature11409 Medline

12. E. Carrington, J. M. Gosline, Mechanical design of mussel byssus: Load cycle and strain rate dependence. *Am. Malacol. Bull.* **18**, 135–142 (2004).

13. M. J. Harrington, A. Masic, N. Holten-Andersen, J. H. Waite, P. Fratzl, Iron-clad fibers: A metal-based biological strategy for hard flexible coatings. *Science* **328**, 216–220 (2010).

doi:10.1126/science.1181044 Medline

14. D. G. Barrett, D. E. Fullenkamp, L. He, N. Holten-Andersen, K. Y. C. Lee, P. B. Messersmith, pH-based regulation of hydrogel mechanical properties through mussel-inspired chemistry and processing. *Adv. Funct. Mater.* **23**, 1111–1119 (2013). doi:10.1002/adfm.201201922 Medline

15. S. C. Grindy, R. Learsch, D. Mozhdehi, J. Cheng, D. G. Barrett, Z. Guan, P. B. Messersmith, N. Holten-Andersen, Control of hierarchical polymer mechanics with bioinspired metal-coordination dynamics. *Nat. Mater.* **14**, 1210–1216 (2015). doi:10.1038/nmat4401 Medline

16. H. Lee, N. F. Scherer, P. B. Messersmith, Single-molecule mechanics of mussel adhesion. *Proc. Natl. Acad. Sci. U.S.A.* **103**, 12999–13003 (2006). doi:10.1073/pnas.0605552103 Medline

17. Z. Xu, Mechanics of metal-catecholate complexes: The roles of coordination state and metal types. *Sci. Rep.* **3**, 2914 (2013). doi:10.1038/srep02914 Medline

18. M. S. Menyo, C. J. Hawker, J. H. Waite, Versatile tuning of supramolecular hydrogels through metal complexation of oxidation-resistant catechol-inspired ligands. *Soft Matter* **9**, 10314–10323 (2013). doi:10.1039/c3sm51824h Medline

19. K.-C. Cheng, Kinetic model of diepoxides with reactive diluents cured with amines. *J. Polym. Sci., B, Polym. Phys.* **36**, 2339–2348 (1998). doi:10.1002/(SICI)1099-0488(19980930)36:13<2339:AID-POLB9>3.0.CO;2-N

20. D. E. Fullenkamp, D. G. Barrett, D. R. Miller, J. W. Kurutz, P. B. Messersmith, pH-dependent cross-linking of catechols through oxidation via Fe(3+) and potential implications for mussel adhesion. *RSC Advances* **4**, 25127–25134 (2014). doi:10.1039/C4RA03178D Medline

21. B. P. Grady, Review and critical analysis of the morphology of random ionomers across many length scales. *Polym. Eng. Sci.* **48**, 1029–1051 (2008). doi:10.1002/pen.21024

22. C. F. Buitrago, D. S. Bolintineanu, M. E. Seitz, K. L. Opper, K. B. Wagener, M. J. Stevens, A. L. Frischknecht, K. I. Winey, Direct comparisons of x-ray scattering and atomistic molecular dynamics simulations for precise acid copolymers and Ionomers. *Macromolecules* **48**, 1210–1220 (2015). doi:10.1021/ma5022117

23. A. J. Lesser, R. S. Kody, A generalized model for the yield behavior of epoxy networks in multiaxial stress states. *J. Polym. Sci., B, Polym. Phys.* **35**, 1611–1619 (1997). doi:10.1002/(SICI)1099-0488(19970730)35:10<1611:AID-POLB13>3.0.CO;2-D

24. E. Hirasawa, Y. Yamamoto, K. Tadano, S. Yano, Effect of metal cation type on the structure and properties of ethylene ionomers. *J. Appl. Polym. Sci.* **42**, 351–362 (1991). doi:10.1002/app.1991.070420207

25. H. J. Qi, M. C. Boyce, Stress-strain behavior of thermoplastic polyurethanes. *Mech. Mater.* **37**, 817–839 (2005). doi:10.1016/j.mechmat.2004.08.001

26. M. A. Bellinger, J. A. Sauer, M. Hara, Tensile fracture properties of rigid-rigid blends made of sulfonated polystyrene ionomer and polystyrene. *Macromolecules* **27**, 6147–6155 (1994). doi:10.1021/ma00099a033

27. L. G. P. Moraes, R. S. F. Rocha, L. M. Menegazzo, E. B. de Araújo, K. Yukimito, J. C. S. Moraes, Infrared spectroscopy: A tool for determination of the degree of conversion in dental composites. *J. Appl. Oral Sci.* **16**, 145–149 (2008). doi:10.1590/S1678-77572008000200012 Medline

28. M. González-González, J. Carlos, J. Baselg, in *Infrared Spectroscopy - Materials Science, Engineering and Technology*, T. Theophile, Ed. (InTech, 2012), pp. 261–284.

29. Y. Li, R. Beck, T. Huang, M. C. Choi, M. Divinagracia, Scatterless hybrid metal-single-crystal slit for small-angle X-ray scattering and high-resolution X-ray diffraction. *J. Appl. Cryst.* **41**, 1134–1139 (2008). doi:10.1107/S0021889808031129

30. S. W. Taylor, D. B. Chase, M. H. Emptage, M. J. Nelson, J. H. Waite, Ferric ion complexes of a DOPA-containing adhesive protein from Mytilus edulis. *Inorg. Chem.* **35**, 7572–7577 (1996). doi:10.1021/ic960514s